Modeling of Aft-Emitted Tonal Fan Noise in Isolated and Installed Configurations

Dimitri Papamoschou *

University of California, Irvine, CA, 92697-3975, USA

The paper presents an initial methodology for low-cost modeling of aft-emitted tonal fan noise in isolated and installed configurations. The theoretical development is done jointly with experimental measurements in an anechoic facility. The model comprises linear coherent partial fields prescribed on a cylindrical surface near the edge of the shear layer formed at the fan exit. The partial fields possess the same axial wavenumbers and azimuthal modes as the aft-propagating duct modes that are cut-on. The shapes of the partial fields are parameterized and the parameter vector is determined by least-squares minimization of the difference between modeled and experimental cross-spectral densities in the far field. In installed arrangements, the emission from the parameterized source is used as the incident field in the computation of scattering using the boundary element method. The experiment utilized a small-scale ducted fan with rotor tip Mach number of 0.59. Microphone measurements with high spatial resolution were enabled by the combination of fixed sensors with one scanning sensor. The recording of a tachometer enabled filtering of the signals into tonal and broadband components, with the focus here on the second harmonic of the blade pass frequency. Integration of a flat plate enabled measurements in a canonical shielded configuration. The results indicate an extended, wavepacket-like nature of the noise source with emission similar to Mach wave radiation from supersonic jets. The model captures the overall directivity of the experimental spectrum and its modification by insertion of the plate.

I. Introduction

The aviation community has set ambitious targets for the development of ultra-quiet subsonic commercial aircraft, encapsulated by NASA's N+2 and N+3 noise goals [1]. Candidate propulsion schemes revolve around the high-bypass turbofan and the open rotor. Attainment of the noise goals requires not only improvements at the component level, but also a systems integration approach for the design of the propulsor and the airframe. A comprehensive review of candidate configurations can be found in Spakovsky [2]. The shielding of engine noise by the airframe has been of particular interest, with efforts addressing fan inlet [3], fan outlet [4], jet [5], and open rotor [6]. The blended wing body (BWB) airplane design has been central to these efforts because its layout is amenable to innovative integration concepts [7].

The development of efficient predictive tools for the emission of the isolated and installed noise source is critical for the design of these advanced aircraft. In this study, the focus is on aft-emitted fan tonal noise. Even though the problem can be addressed using sophisticated computational techniques (for example, Refs. [8, 9]), there is desirability of low-cost models that can provide rapid turnaround with sufficient accuracy. Once a reliable source model is developed, the scattering of the emitted sound can be predicted using techniques such as the boundary element method [10] or the equivalent-source method [11].

This paper presents preliminary results on a surface-based source model for the aft-emitted fan tonal noise that is informed by key features of the internal pressure field. The primary purpose of the model is prediction of the installed emission given knowledge of the isolated acoustics. The model is developed with the aid of experimental measurements of the noise emitted by a small-scale ducted fan. The experiment featured a phased array that comprised fixed and continuously-scanning sensors. The continuous-scan approach [12–14] in the measurement of the acoustic field provides superior spatial resolution needed in the model validation. The model emission is integrated with the BEM to provide scattering predictions for canonical installed configurations. A companion paper presents additional results and alternative treatments for the prediction of isolated and installed noise [15].

---

*Professor, Department of Mechanical and Aerospace Engineering, Fellow AIAA.

II. Experimental Details

A. Ducted Fan Setup

At the UCI Aeroacoustics Laboratory, a small-scale ducted fan simulated the fan noise emission of a high-bypass turbofan engine. The ducted fan rig is shown in Fig. 1a, and its detailed design has been documented in Ref. [16]. The nacelle has inlet diameter of 70 mm and exit-to-inlet area ratio of 0.56. The fan outlet diameter is D_o=74 mm. The overall design is based on the GE R4 fan with a rotor blade count of 14 and stator vane count of 24. The design includes a pylon and bifurcation as in a typical turbofan engine. Powered by a 6-hp DC brushless motor, the fan develops a pressure ratio FPR = 1.15 and tip Mach number of 0.59 when it rotates at 55500 RPM. This rotational speed was held to within ~1% in the experiments described here. The exit flow Mach number was $M = 0.45$, and it is assumed that the flow inside the duct near the exit was at approximately the same Mach number. In the installed configuration, Fig. 1b, a rectangular flat plate with span of 610 mm, chord length of 305 mm, and thickness of 3.2 mm was placed near the fan. The plate was located at a height of 65 mm from the fan centerline and its trailing edge was positioned at $X_{\text{TE}} = 55$ and 78 mm from the fan exit plane ($X_{\text{TE}}/D_o = 0.74$ and 1.05, respectively). See also Fig. 3.

(a)   **(b)**
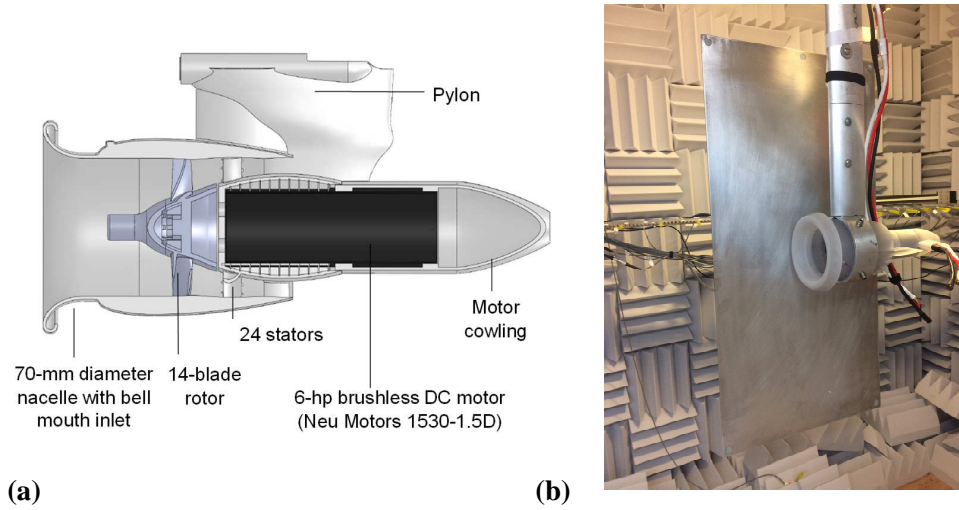
Fig. 1   Small-scale ducted fan rig. (a) Schematic; (b) installation with plate.

B. Diagnostics

Acoustic measurements were performed in the anechoic chamber depicted in Fig. 2 using 23 fixed and one continuously-scanning Bruel & Kjaer Type 4138 microphones, with frequency response up to 120 kHz. The polar angle θ is defined relative to the downstream axis and the distance of the sensors R is measured from the center of the fan exit plane. All the fixed microphones were mounted on a linear inclined holder and covered the polar aperture $26° \leq \theta \leq 121°$. The scanning microphone traversed along the line of the fixed sensors with a lateral offset of 6 mm. Its polar aperture was $32° \leq \theta \leq 73°$. The non-dimensional sensor distance R/D_o ranged from 12.3 to 20.3.

The microphones were sampled simultaneously at a rate of 250 kS/s per channel by six National Instruments PCI-6143 data acquisition boards installed in a desktop computer. The scan speed was 76.2 mm/s and the experimental duration was 12 s over which 3000000 samples were acquired. Positioning of the scanning microphone was determined from the encoder signal of the motor powering the traverse and was verified by a laser displacement sensor. Details of the scanning setup can be found in Refs. [13, 14]. In addition to the microphones, a tachometer measured the rotational speed of the rotor and Pitot probes measured the total pressure at the fan exit.
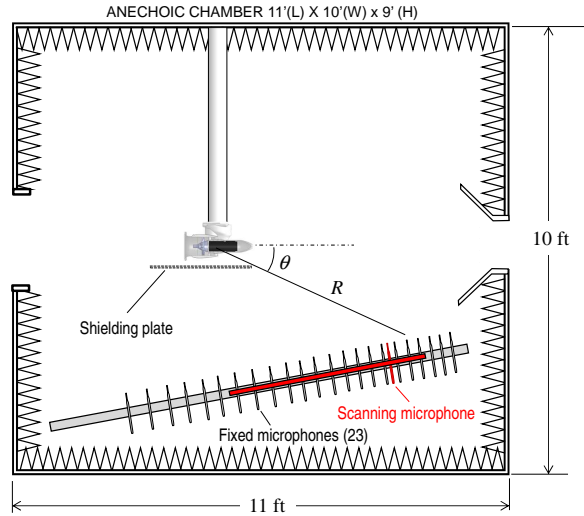
Fig. 2   Anechoic chamber setup.

C. Signal Processing

Spectral densities were computed with Fast Fourier Transform (FFT) size of 2048, yielding a frequency resolution of 122 Hz. Sound pressure level (SPL) spectra, at polar angle $\theta = 49.4°$ are plotted in Fig. 3 for the isolated and shielded configurations. The fundamental blade passing frequency (BPF) was near 13.0 kHz. Tones up to the sixth harmonic are evident in the plots. It is notable that the plate reduces broadband noise significantly, but not all the tonal levels. For certain polar-angle ranges some tones actually amplify.
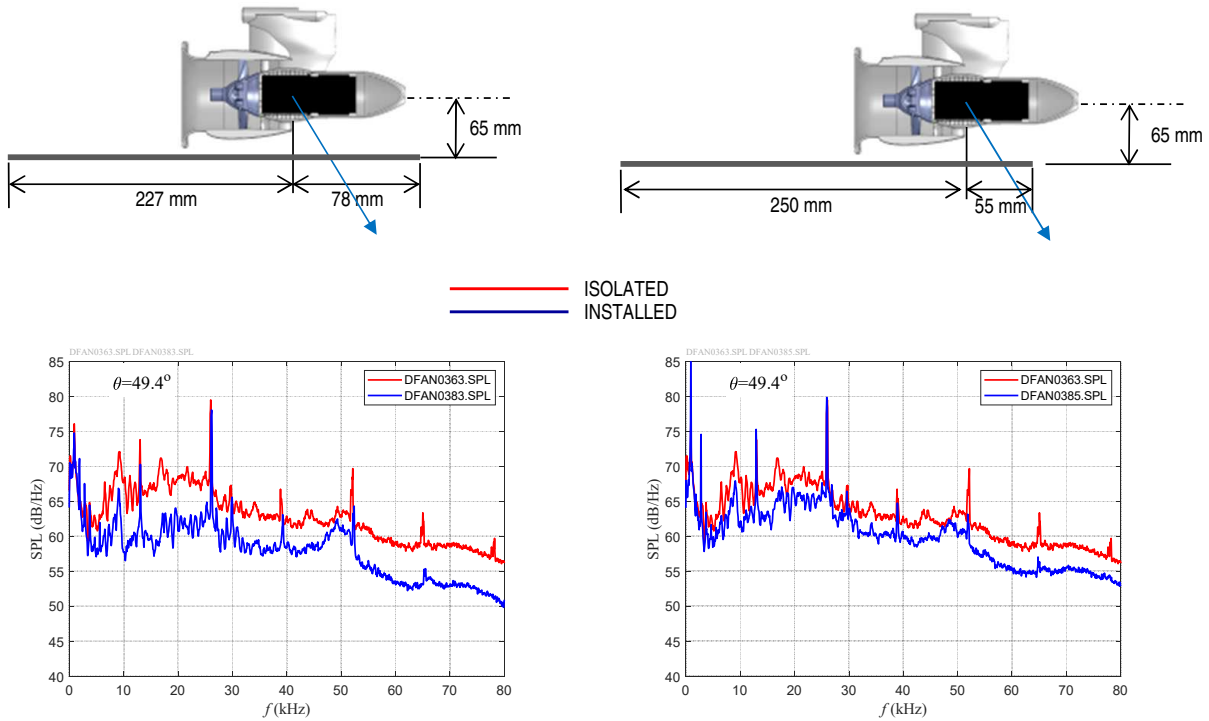
Fig. 3   Narrowband SPL spectra at polar angle $\theta = 49.4°$ for the isolated and installed configurations.

3

The focus of this project being on tonal noise, the Vold-Kalman filter [17–19] was used to separate the tonal (harmonic) and broadband content, aided by the tachometer measurement. A typical separation is presented in Fig. 4. The power spectral density (PSD) of each harmonic is defined as the integral of the harmonic spectrum centered around the tone frequency (that is, the area under a given spike). Similarly, the cross-spectral density (CSD) of each harmonic is the integral of the harmonic part of the cross-spectrum centered at the tone frequency.
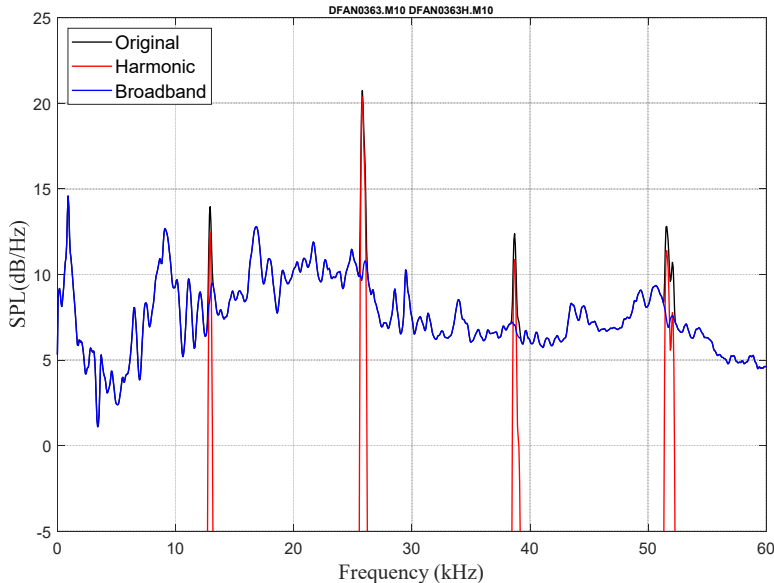
Fig. 4   Example of Vold-Kalman filtering: spectral densities of original signal and its harmonic and broadband components.

Use of the scanning microphone requires division of the signals into a number of relatively short blocks, then correlating the fixed and scanning microphone signals for each block [14]. Here 70 blocks were used, each containing 131072 samples, with overlap of 67%. When computing the tone amplitude for each block, it was noted that the amplitude varied substantially from block to block (i.e., with time). To mitigate this effect the harmonic signal was detrended by dividing it by the short-time (10-ms window) rms and multiplying it by the long-time (2s-window) rms. Beamforming using the Bayesian coherence-based estimation technique of [20] was performed for two array apertures, one covering low polar angles and the other covering high polar angles. Imaging at low polar angle showed only one source location near the fan exit plane. The image at large polar angle showed also a distinct contribution from the fan inlet. Given that the focus of this project is aft tonal emission, the polar angle range of interest was confined to less than 75° to minimize the influence of the inlet.

III. Model for Aft Tonal Emission

A. Fundamentals

The noise source model for aft tonal emission is defined as a collection of coherent partial fields prescribed on a near-field surface, as drawn in Fig. 5a. This concept is inspired by earlier efforts to model the jet noise source and its diffraction [10, 21], the difference here being that the tonal noise is deterministic (versus the randomness of the jet turbulence). An initial effort in this direction can be found in Ref. [22]. The source surface is a circular cylinder with radius $r = r_{source}$. The axial coordinate x is zero at the fan exit plane. A central assumption in the model is that the partial fields retain key characteristics of the sound propagation inside the duct.

4
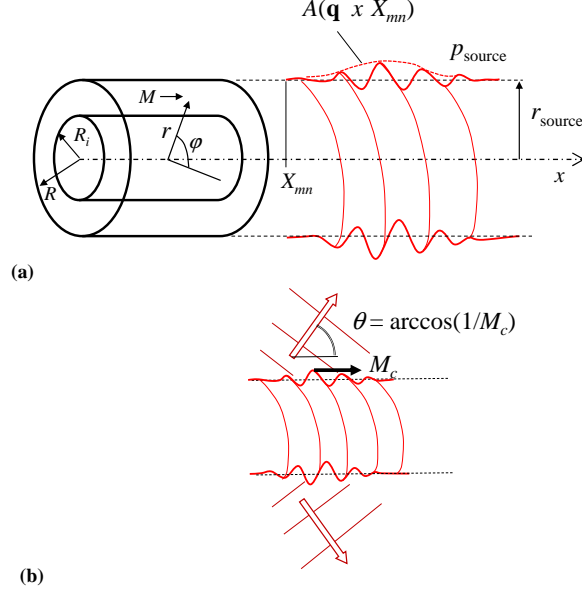
Fig. 5   (a) Surface-based source model for aft tonal emission; (b) illustration of Mach wave radiation.

B. Internal Pressure Field

The relations for the internal pressure field follow those in Redonnet and Druon [9]. Consider an annular duct with outer radius R_o, inner radius R_i, and uniform mean Mach number M, as shown in Fig. 5a. The solution of the wave equation inside the duct at radian frequency ω gives the aft-propagating pressure field

$$p_{in}(x, r, \phi, t) = \sum_{m=-\infty}^{\infty} \sum_{n=0}^{\infty} C_{mn} D_{mn}(k_{r_{mn}} r) e^{i(k_{x_{mn}} x + m\phi - \omega t)} \tag{1}$$

The total field is a sum of modes, each mode defined by the product of the separable radial, axial and azimuthal eigenfunctions: D_{mn}, $e^{ik_{x_{mn}} x}$, and $e^{im\phi}$. The complex coefficient C_{mn} sets the amplitude and phase of each field associated with azimuthal mode number m and radial mode n, where possible values of these integers are indicated in the summation limits. The axial and radial wavenumbers, $k_{x_{mn}}$ and $k_{r_{mn}}$, are constrained by the dispersion relation

$$k_{x_{mn}} = \frac{k}{1 - M^2} \left\{ -M + \sqrt{1 - (1 - M^2) \left(\frac{k_{r_{mn}}}{k} \right)^2} \right\} \tag{2}$$

where $k = \omega/a$ is the acoustic wave number and a is the ambient speed of sound. For a given frequency, the value of the radial wavenumber determines whether the axial wavenumber is real or imaginary. It is evident from Eq. 1 that a real $k_{x_{mn}}$ results in a propagating wave while an imaginary $k_{x_{mn}}$ results in exponential decay. Available radial wavenumbers are set by the hardwall boundary condition

$$J_m'(k_{r_{mn}} R_i) \, Y_m'(k_{r_{mn}} R_o) - J_m'(k_{r_{mn}} R_o) \, Y_m'(k_{r_{mn}} R_i) = 0 \tag{3}$$

where J_m' and Y_m' are the derivatives of the Bessel functions of the first and second kind, respectively, and of order m.

For a fan with a rotor containing B blades the radian frequency is $\omega = n_{\text{BPF}} B \Omega$ where Ω is the shaft angular velocity and n_{BPF} tak2es values of positive integers (1, 2, . . .) and represents the fundamental blade pass tone and higher harmonics. Including the interaction with a row of stators containing V vanes, per the analysis of Tyler and Sofrin [23] azimuthal mode numbers are constrained to be sums of integer combinations of rotor and stator counts, i.e.,

$$m = n_{\text{BPF}} B + jV \quad , \qquad \begin{array}{l} n_{\text{BPF}} = 1, 2, \ldots \\ j = \ldots, -2, -1, 0, 1, 2, \ldots \end{array} \tag{4}$$

5

Combining Eqs. 2,3, and 4, one determines the axial wavenumber for each n_{BPF} and j. Modes (m,n) for which $k_{x_{mn}}$ is real, and thus disturbances propagate, are referred to as cut-on; while modes for which $k_{x_{mn}}$ is imaginary, and thus disturbances decay, are referred to as cut-off. For the cut-on modes, the speed of propagation (convection) is $\omega/k_{x_{mn}}$. The criterion for sound propagation in the duct is summarized as follows:

$$
\begin{aligned}
k_{r_{mn}}\sqrt{1-M^2} &< k \quad : \text{mode is CUT-ON} \\
k_{r_{mn}}\sqrt{1-M^2} &\geq k \quad : \text{mode is CUT-OFF}
\end{aligned}
\tag{5}
$$

C. External Source

It is now assumed that the surface-based source outside the duct comprises partial fields that have the same axial wavenumbers $k_{x_{mn}}$ and same azimuthal modes m as the cut-on modes inside the duct. As indicated in Fig. 5a, the partial fields are modulated by an amplitude $A(\mathbf{q},x)$, where $\mathbf{q}$ is a parameter vector that controls the shape of the function. Associated with each partial field is the convective Mach number

$$
M_{c_{mn}} = \frac{k}{k_{x_{mn}}}
\tag{6}
$$

In analogy with Mach wave emission in supersonic jets, the convective Mach number can be connected to the direction of polar emission via

$$
\theta_{mn} = \arccos\left(\frac{1}{M_{c_{mn}}}\right)
\tag{7}
$$

as seen in Fig. 5b, where θ is the polar angle from the downstream axis. This relation does not account for the amplitude modulation of the partial field or its helical content; however, it it expected to provide a fair estimate of the emission angle. Computational results of aft fan noise emission by Huang *et al.* [8] show an emission pattern similar to Mach wave emission in jets that motivates the current approach.

On $r = r_{\text{source}}$, the surface-based source is defined by:

$$
p_{\text{source}}(\mathbf{q}, B_{mn}; x, \phi, t) = e^{-i\omega t} \sum_{(m,n)\in G} B_{mn}\, p_{mn}(\mathbf{q}; x - X_{mn}, \phi)
\tag{8}
$$

In the above equation $(m,n) \in G$ is the set of cut-on modes, B_{mn} are the amplitudes of the modes, and X_{mn} are the axial origins of the partial fields. The coherent partial fields are given by

$$
p_{mn}(\mathbf{q}; x - X_{mn}, \phi) = A(\mathbf{q}; x - X_{mn})e^{i[k_{x_{mn}}(x-X_{mn})+m\phi]}
\tag{9}
$$

$\mathbf{q}$, B_{mn}, and X_{mn} are free parameters that are tuned to match the measured data. Each partial field p_{mn} is propagated to a field point $\mathbf{x}_i = (x, r, \phi)$ outside the source cylinder. For the cylindrical source surface considered here, the solution to the wave equation gives the emitted pressure field [21]

$$
P_{mn}(\mathbf{q}, X_{mn}; \mathbf{x}_i, t) = \frac{1}{2\pi}e^{-i\omega t}\int_{-\infty}^{\infty} \widehat{p}_{mn}(\mathbf{q}, \kappa_x, \phi)\frac{H_m^{(1)}(\kappa_r r)}{H_m^{(1)}(\kappa_r r_{\text{source}})}e^{i\kappa_x(x-X_{mn})}d\kappa_x
\tag{10}
$$

Here κ_x and κ_r are the axial and radial wavenumbers associated with the outward propagation, respectively, and they are related to the acoustic wavenumber through $k^2 = \kappa_x^2 + \kappa_r^2$; $\widehat{p}_{mn}$ is the axial Fourier transform of p_{mn}; and $H_m^{(1)}$ is the Hankel function of the first kind of order m. Equation 10 was computed using forward and inverse Fast Fourier Transforms (FFTs) enabling rapid evaluation of P_{mn}. The complete pressure field off the source cylinder is obtained from the superposition

$$
p(\mathbf{q}, B_{mn}, X_{mn}; \mathbf{x}_i, t) = \sum_{(m,n)\in G} B_{mn}\, P_{mn}(\mathbf{q}, X_{mn}; \mathbf{x}_i, t)
\tag{11}
$$

The cross-spectral density at field points $\mathbf{x}_i$ and $\mathbf{x}_j$ is

$$
G_{ij}(\mathbf{q}, B_{mn}, X_{mn}) = p(\mathbf{q}, B_{mn}, X_{mn}\,;\,\mathbf{x}_i, t)\, p^*(\mathbf{q}, B_{mn}, X_{mn}\,;\,\mathbf{x}_j, t)
\tag{12}
$$

Table 1. Cut-on modes for $n_{BPF} = 2$

(m,n)	(4,1)	(4,2)
k_x (m^{-1})	308.7	178.6
M_c	1.530	2.644
θ (deg)	49.2	67.8

where * denotes the complex conjugate. The combined parameter vector

$$\mathbf{V} = [\mathbf{q}; B_{mn}; X_{mn}] \tag{13}$$

is obtained by minimizing the cost function

$$F(\mathbf{V}) = \left\| \frac{G_{ij}(\mathbf{V})}{G_{max}(\mathbf{V})} - \frac{G_{exp,ij}}{G_{exp,max}} \right\|_2 + \mathcal{P}(\mathbf{V}) \tag{14}$$

where $G_{exp,ij}$ is the experimental cross-spectral density, G_{max} is the maximum value of the modeled autospectral density, and $G_{exp,max}$ is the maximum value of the experimental autospectral density. The normalizations in Eq. 14 mean that the modeled and experimental cross-spectral densities are matched (in a least-squares sense) up to a multiplicative constant, the ratio $G_{max}(\mathbf{V})/G_{exp,max}$. The component $\mathcal{P}(\mathbf{V})$ is a penalty function that forces an errant element of the vector to return to within a reasonable range. The bounds in the penalty function were set wide; at the conclusion of the minimization all the parameters fell well within those bounds and thus the penalty function was always zero. The minimization was done using the conjugate gradient algorithm of Shano and Phua [24]. The specific amplitude modulation shape, used in past surfaces-based noise models [21], was selected as

$$A(\mathbf{q}, x) = \tanh(q_1 x)^{q_3} [1 - \tanh(q_2 x)^{q_4}] \tag{15}$$

D. Application to Experiments

The UCI fan rig pictured in Fig. 1 has rotor-stator combination of B=14 and V=24. The duct terminates with an inner radius $R_i = 0.0273$ m and outer radius $R_o = 0.0370$ m. As mentioned in Section II.A, the Mach number inside the duct is approximated as $M = 0.45$. The radius of the source surface is placed at $r_{source} = R_o$. Considering the convergence of the cowl lines past the fan exit plane, a cylindrical surface of radius R_o is expected to be near the edge of or outside the vortical region of the flow. In this study we consider only the second harmonic, $n_{BPF} = 2$. Using the analysis of Eqs. 2-4 it was determined that only modes (4,1) and (4,2) were cut-on. Table 1 lists the corresponding values of the axial wavenumber, convective Mach number, and emission polar angle.

The parameter vector comprised the elements

$$\mathbf{V} = [q_1, q_2, q_3, q_4, B_{4,1}, B_{4,2}, X_{4,1}, X_{4,2}]$$

Given that the B amplitudes are complex, the total number of parameters was 10. However, because the final results are normalized by the maximum value of the power spectral density, the amplitude of the mode expected to be dominant (in this case, mode (4,1)) is set to $B_{4,1} = 1 + 0i$, thus reducing the size of the parameter vector to eight.

The conjugate-gradient minimization of Eq. 14 allows estimation of the parameter vector $\mathbf{V}$ and thus the shapes of the partial fields. Table 2 displays the values of the parameters and Fig. 6 plots the corresponding partial fields. Figures 7 and 8 compare the experimental and modeled cross-spectral density (CSD) and power spectral density (PSD), respectively. The spectral results are normalized by the peaks of their respective autospectra. The modeled PSD, presented in decibel scale, follows well the directivity of the experimental one, showing a primary peak at $\theta \approx 48°$ and a secondary peak at $\theta \approx 65°$, values in line with the theoretical prediction of Table 1. For polar angles above $\theta \approx 70°$ inlet noise starts making an impact. Although showing definite trends, the directivity of the experimental tone is not smooth, which complicates the fit by the model. Non-smoothness of the spatial distribution of fan tones has been observed in earlier experiments with fine spatial resolution [12]. The non-stationarity of the tones noted in Section II.C

Table 2. Parameter vector

q_1	=	$24.0 \ \text{m}^{-1}$
q_2	=	$10.2 \ \text{m}^{-1}$
q_3	=	1.46
q_4	=	1.82
$B_{4,1}$	=	1.000
$B_{4,2}$	=	$0.200 e^{i \ 2.90}$
$X_{4,1}$	=	$0.013 \ \text{m}$
$X_{4,2}$	=	$0.000 \ \text{m}$

also contributes to the jaggedness of the distributions that involve the scanning sensor. The modeled CSD captures the oscillation and overall trends of the experimental one. The cost function of Eq. 14 was minimized to 0.18 for the complete cross-spectral density and 0.14 for the autospectral component. The richness of the information enabled by the continuous-scan paradigm is evident in the spectral figures. Without the scanning microphone, the polar resolution would have been about 4°. With the scanning microphone, the polar resolution is approximately 0.5°. It is clear that many features of the cross- and auto-spectra would be missed if only the fixed sensors were used.
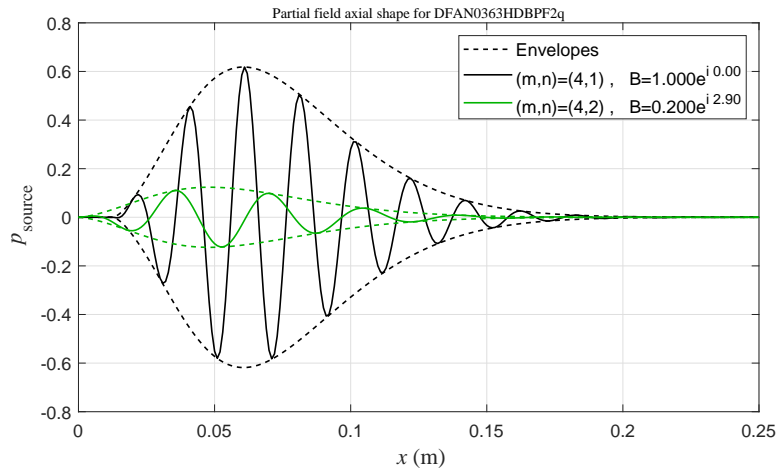
Fig. 6 Partial fields of source for $n_{\text{BPF}} = 2$.

8
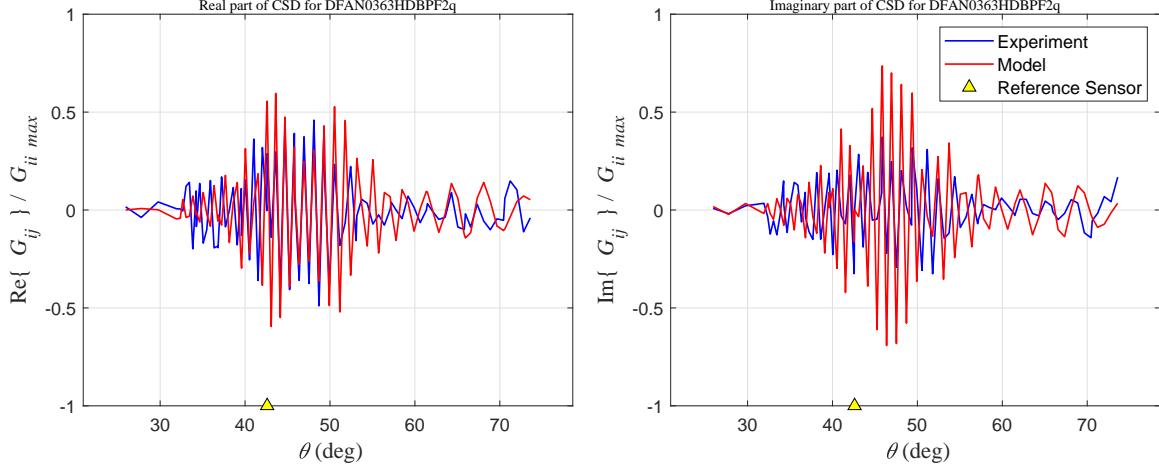
Fig. 7 Real (left) and imaginary (right) polar distributions of the experimental and modeled cross-spectral densities for $n_{\mathrm{BPF}} = 2$ with the reference microphone at $\theta = 42°$.
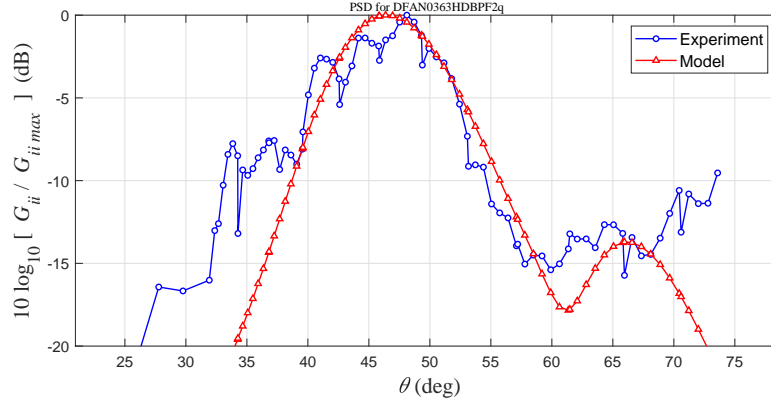
Fig. 8 Polar distributions of the experimental and modeled power spectral densities for $n_{\mathrm{BPF}} = 2$.

IV. Prediction of Installed Emission

The near-field surface source model generated the incident field for computing the diffraction around the plate installed near the ducted fan. The numerical plate had the same dimensions and placement as the experimental one. The diffraction from the parameterized source was computed using the Fast Multipole BEM [25] (FastBEM software, Advanced CAE Research, LLC). The non-dimensional wavenumber based on chord length was $kc = 145$. The computation used a triangular mesh with density of six elements per wavelength. Approximately 100000 boundary elements were used for the second-harmonic frequency of 26 kHz. Meshing was automated and the plate was remeshed for every position of the plate (the coordinate system was always fixed with the fan exit plane). The incident field at the boundary and field points was computed from Eq. 10 using forward and inverse FFTs, a process that took approximately 20 min on a standard laptop. The BEM computation took approximately 60 min of wall time.

Comparisons between the modeled and experimental PSDs are shown in Figs. 9 and 10 for X_{TE}=78 mm and 55 mm, respectively. For each set of comparisons, the spectra are normalized by the peak value of the isolated spectrum and the results are presented in decibels. For X_{TE}=78 mm the experiment shows PSD reduction of 3-10 dB at low polar angles, and around 2.5 dB at the angle of peak emission $\theta = 48°$. Above this angle, the reduction becomes small with an angle range where the installed tonal noise is higher than the isolated one. The model predicts relatively well the reduction in peak emission and the cross-over at large polar angle; it does not capture the reduction at small angles. For the shorter shield length in Fig. 10 the experiment and model are in agreement on the very modest noise reduction. The results of Figs. 9 and 10 indicate that the source of tonal noise is extended and thus not easy to shield. The extended nature of

9

the source is compatible with the partial field model used here. It is notable that a shield length slightly shorter the fan exit diameter provided minimal tonal suppression, even though the broadband noise was reduced significantly (Fig. 3).
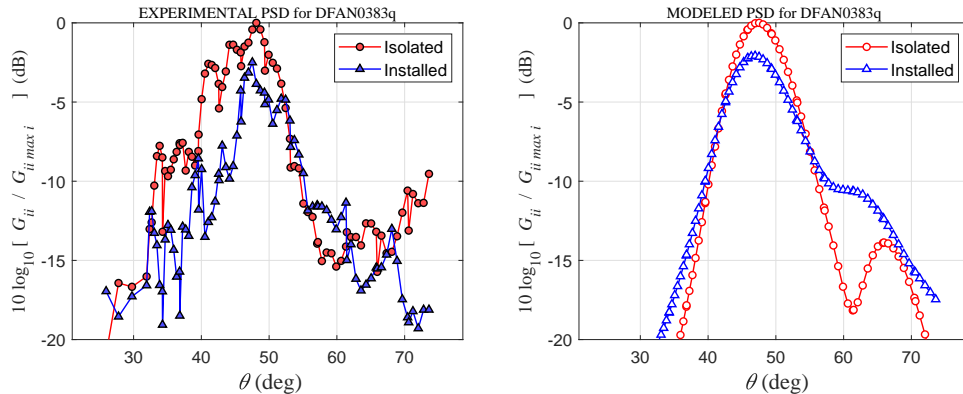
Fig. 9 Polar distributions of the isolated and installed spectral densities for $n_{BPF} = 2$ and X_{TE}=78 mm. Left: experiment. Right: model
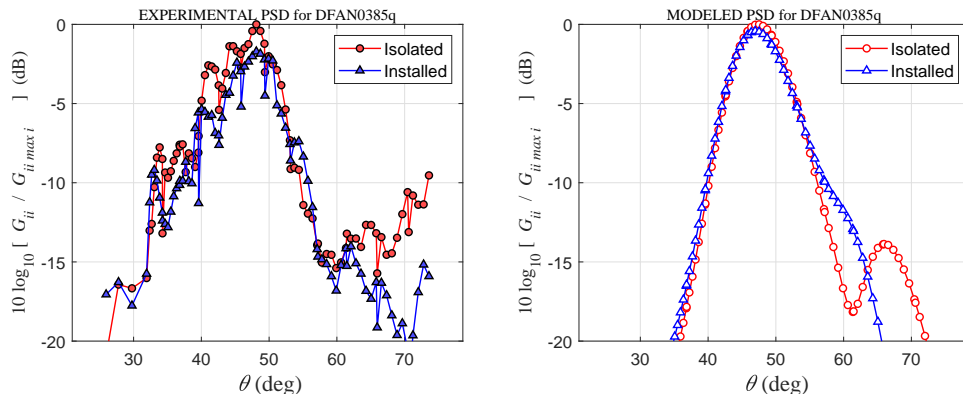
Fig. 10 Polar distributions of the isolated and installed spectral densities for $n_{BPF} = 2$ and X_{TE}=55 mm. Left: experiment. Right: model

V. Concluding Remarks

The paper presented a coupled theoretical and experimental effort aimed at developing low-cost models of aft-emitted tonal fan noise in isolated and installed configurations. The source model is prescribed on a near-field cylindrical surface in the form of linear coherent partial fields with axial wavenumbers and azimuthal modes equal to those of the aft-propagating duct modes that are cut-on. The shapes and amplitudes of the partial fields are parameterized, and the parameter vector is determined by least-squares minimization of the difference between modeled and experimental cross-spectral densities in the far field. In installed arrangements, the emission from the parameterized source is used as the incident field for the prediction of scattering using the boundary element method. The experiment used a small-scale ducted fan and microphone measurements with high spatial resolution enabled by the combination of fixed sensors with one scanning sensor. Harmonic-broadband separation utilized the Vold-Kalman filter, and the focus was placed on the second harmonic of the blade pass frequency. Integration of the ducted fan with a rectangular plate enabled measurements in a canonical shielded configuration. The results indicate an extended, wavepacket-like nature of the noise source with emission similar to Mach wave radiation from supersonic jets. The model captures the overall directivity of the experimental spectrum and its modification by insertion of the plate. The extended nature of the tonal source makes effective shielding more challenging than for broadband noise.

The assumption that the external source retains the same axial wavenumbers and azimuthal modes as the internal cut-on modes appears to be supported by the experimental measurements but needs to be solidified by detailed near-field

measurements and theoretical analysis. It is also possible that this relation may become less constrained by simply inferring the convective Mach numbers (and therefore axial wavenumbers) by the polar directivity of the tonal peaks in the far field.

There are additional, realistic features that need to be included such as the effect of the bifurcation that complicates the Tyler-Sofrin mode selection of Eq. 4. The jagged spatial distribution and non-stationarity of the tonal content present challenges for the modeling. The relevance of these complications needs to be assessed in relation to their impact on flyover perceived noise. If they do not impact perceived noise, appropriate smoothing and averaging of the experimental data will facilitate the modeling.

Several features of the model can be readily generalized. The source surface does not need to be cylindrical; in fact, a convergent conical-like surface may be more appropriate given the convergence of the cowl lines and exhaust slipstream in a realistic engine [26]. The cylindrical surface enables a relatively simple analytical expression for the emitted field (Eq. 10). Emission from more complex surfaces can be handled using the BEM, which may provide faster solutions than the FFT treatment of Eq. 10. Preliminary work indicates that this is indeed the case, therefore both the emission and the scattering can be computed with the BEM. The BEM would also permit more complex models of the partial fields that would include the effect of the bifurcation as it is treated for the internal field [9].

The present paper discussed only the second harmonic due to time and resource limitations. Clearly, the model needs to be extended to and validated for all the relevant harmonics. Higher harmonics will contain richer modal content, motivating the need to constrain the size of the parameter vector of Eq. 12. The experimental tonal directivity may provide guidance as to which modes are relevant.

References

[1] Jones, S., Haller, W., and Tong, M., "An N+3 Technology Level Reference Propulsion System," *NASA/TM-2017-219501*, 2017.

[2] Spakovsky, Z., "Advanced Low-Noise Aircraft Configurations and their Assessment: Past, Present, and Future," *CEAS Aeronautical Journal*, Vol. 10, 2019, pp. 137–155. doi:10.1007/s13272-019-00371-8.

[3] Gerhold, C., Clark, L., Dunn, M., and Tweed, J., "Investigation of Acoustical Shielding by a Wedge-Shaped Airframe," *Journal of Sound and Vibration*, Vol. 294, No. 1-2, 2006, pp. 49–63. doi:10.1016/j.jsv.2005.10.010.

[4] Chappuis, J., Ricouard, J., and Roger, M., "Aft Fan Noise Shielding by a Lifting Surface: Analytical, Numerical, and Experimental Results," *AIAA Paper 2006-2617*, 2006. doi:10.2514/6.2006-2617.

[5] Thomas, R., Burley, C., and Olson, E., "Hybrid Wing Body Aircraft System Noise Assessment with Propulsion Airframe Aeroacoustic Experiments," *International Journal of Aeroacoustics*, Vol. 11, 2012. doi:10.1260/1475-472X.11.3-4.369.

[6] Berton, J., "Empennage Noise Shielding Benefits for an Open Rotor Transport," *AIAA Paper 2011-2764*, 2011. doi:10.2514/6.2011-2764.

[7] Liebeck, R., "Design of the Blended Wing Body Subsonic Transport," *Journal of Aircraft*, Vol. 41, No. 1, 2004, pp. 10–25. doi:10.2514/1.9084.

[8] Huang, X., Chen, Z., Ma, Z., and Zhang, X., "Efficient Computation of Spinning Modal Radiation Through an Engine Bypass Duct," *AIAA Journal*, Vol. 46, No. 6, 2008, pp. 1413–1423. doi:10.2514/1.31136.

[9] Redonnet, S., and Druon, Y., "Computational Aeroacoustics of Aft Fan Noise Characterizing a Realistic Coaxial Engine," *AIAA Journal*, Vol. 50, No. 5, 2012, pp. 1029–1046. doi:10.2514/1.J050730.

[10] Papamoschou, D., "Prediction of Jet Noise Shielding," *AIAA Paper 2010-0653*, 2010. doi:10.2514/6.2010-653.

[11] Nark, D., Burley, C., Tinetti, A., and Rawls, J., "Initial Integration of Noise Prediction Tools for Acoustic Scattering Effect," *AIAA Paper 2008-2996*, 2009. doi:10.2514/6.2008-2996.

[12] Shah, P., Vold, H., Hensley, D., Envia, E., and Stephens, D., "A High-Resolution Continuous-Scan Acoustic Measurement Method for Turbofan Engine Applications," *Journal of Turbomachinery*, Vol. 137, 2015, pp. 121002–121002–11. doi: 10.1115/1.4031341.

[13] Shah, P., Lee, A., Hensley, D., Schweizer, L., Yang, M., and Papamoschou, D., "Continuous-Scan Phased Array Measurement Methods for Turbofan Engine Acoustic Testing," *Journal of Engineering for Gas Turbines and Power*, Vol. 141, No. 8, 2019, pp. 081201–081201–13. doi:10.1115/1.4042395.

[14] Papamoschou, D., Morata, D., and Shah, P., "Inverse Acoustic Methodology for Continuous-Scan Phased Arrays," *AIAA Journal*, Vol. 57, No. 2, 2019, pp. 5126–5140. doi:10.2514/1.J058085.

[15] Shah, P., Lee, A., Hensley, D., Schweizer, L., Yang, M., and Papamoschou, D., "Toward Efficient Propulsion Airframe Aeroacoustic Prediction Using High-Resolution Source Characterization and Modeling," *AIAA Scitech Forum*, 2021.

[16] Truong, A., and Papamoschou, D., "Experimental Simulation of Ducted Fan Acoustics at Very Small Scale," *AIAA Paper 2014-0718*, 2014. doi:10.2514/6.2014-0718.

[17] Vold, H., and Leuridan, J., "High Resolution Order Tracking at Extreme Slew Rates Using Kalman Tracking Filters," *SAE Technical Paper 931288*, 1993. doi:10.4271/931288.

[18] Stephens, D., and Vold, H., "Order Tracking Signal Processing for Open Rotor Acoustics," *Journal of Sound and Vibration*, Vol. 333, 2014, pp. 3818–3830. doi:10.1016/j.jsv.2014.04.005.

[19] Truong, A., and Papamoschou, D., "Harmonic and Broadband Separation of Noise from a Small Ducted Fan," *AIAA Paper 2015-3282*, 2015. doi:10.2514/6.2015-3282.

[20] Papamoschou, D., "Imaging of Distributed Directional Noise Sources," *Journal of Sound and Vibration*, Vol. 330, No. 10, 2011, pp. 2265–2280. doi:10.1016/j.jsv.2010.11.025.

[21] Papamoschou, D., "Wavepacket Modeling of the Jet Noise Source," *International Journal of Aeroacoustics*, Vol. 17, No. 1-2, 2018, pp. 52–69. doi:10.1177/1475472X17743653.

[22] Truong, A., "Experimental and Theoretical Investigation of the Emission and Diffraction of Discrete Tone Noise Generated from the Exhaust of a Ducted Fan," *Ph.D Thesis, University of California, Irvine*, 2018.

[23] Tyler, J., and Sofrin, T., "Axial Flow Compressor Noise Studies," *SAE Transactions*, Vol. 70, 1962, pp. 309–332. doi:10.4271/620532.

[24] Shanno, D. F., and Phua, K. H., "Minimization of Unconstrained Multivariate Functions," *ACM Transactions on Mathematical Software*, Vol. 6, No. 4, 1976, pp. 618–622. doi:10.1145/355666.355673.

[25] Liu, Y., "Fast Multipole Boundary Element Method: Theory and Applications in Engineering," Cambridge University Press, Cambridge, 2009. doi:10.1017/CBO9780511605345.

[26] Goulos, I., MacManus, D., and Sheaf, C., "Civil Turbofan Engine Exhaust Aerodynamics: Impact of Fan Exit Flow Characteristics," *Aerospace Science and Technology*, Vol. 93, 2019, pp. 1–12. doi:10.1016/j.ast.2019.05.033.